

Carbons-to-SiO_x Contact Ratio for Faster Graphite/SiO_x Electrode Formulation Optimization

Clément Meyssonnier,^[a, b] Cassandre Chalard,^[a, b] Nicolas Goubard-Bretesché,^[a] Amina Merabet,^[a] Nicolas Dupré,^[a] Cyril Paireau,^[b] and Bernard Lestriez*^[a]

The optimization of composite electrodes based on a silicon/graphite mixture is essential for battery performance, but is complex due to the multiplicity of parameters that come into play. In this direction, we propose to adjust the amount of surface area developed by all the graphitic carbons, including the conductive additive to that of the silicon phase. This concept, introduced here as graphite and carbon-to-silicon contact ratio, is based on the importance of contacts on the mechanical, electrical and electrochemical properties of compo-

site electrodes. The validity of this new formulation parameter is studied here for SiO_x/Graphite composite electrodes, which differ in the proportions of two types of graphite (spherical or platelet form) and for different types of conductive additives (carbon black and carbon nanotubes). An optimal contact ratio is determined, allowing at the same time the best gravimetric and volumetric capacities, the best cyclability, and the best power performance.

Introduction

Silicon/Graphite blends are the subject of intense research and development with the aim of increasing the volume energy density of Li-ion batteries.^[1] Silicon indeed has many assets: (i) it is abundant, eco-friendly, and non-toxic, (ii) it offers very high gravimetric and volumetric capacities (3579 mAh g⁻¹ and 2194 mAh cm⁻³, respectively, at room temperature (RT)), and (iii) it displays an appropriate average voltage of ca. 0.4 V vs. Li⁺/Li. However, silicon suffers from poor cyclability due to the large volume change when alloying with lithium (280% during full-capacity cycling at RT), leading to subsequent mechanical and chemical degradation. It is most often used in an oxidized form (SiO_x) and/or intimately combined with carbon or graphite in the form of a composite material (Si@C or Si@G), or even combined in the form of an alloy with inactive elements (Si@M).^[2] In the rest of this introduction all these silicon-based materials will be referred to indifferently as silicon and for certain examples their exact composition will be specified.

In electrodes based on silicon/graphite blends, graphite plays the role of both active material and conductive agent, and buffers the volume expansion of the silicon. The aging mechanisms of these electrodes are: (i) due to irreversible expansion of the electrode, the loss of contact between the particles of silicon and graphite or conductive additive, and therefore the inactivation of the silicon by the disruption of the electron supply; (ii) the loss of contact between the electrode

and the current collector due to mechanical stresses at their interface; (iii) the continued growth of the SEI which consumes the electrolyte (solvents and lithium salt), blocks the porosity of the electrode, and electrically insulates the silicon surface; and finally (iv) the growth of the impedance of the electrode due to the phenomena mentioned above.^[3–9] The extent of these mechanisms is modulated by the nature of the silicon-based material (SiO_x, Si@C, Si@G, Si@M) and by its quantity in the electrode. In addition, each type of silicon has its own aging mechanisms at the particle scale.

The complexity of such a system compels a thorough understanding of the interactions between silicon and graphite, how these influence the electrical, mechanical, and electrochemical behaviors of the electrodes, in order to optimize their performance. The first parameter is the silicon vs. graphite ratio. In general, increasing the silicon content degrades the cyclability of the electrodes.^[4,10] The morphology of the electrode plays a crucial role. If the silicon is agglomerated, its volume expansion is intensified, thus leading to greater swelling of the electrode, accelerating the capacity fading due to loss of mechanical contact.^[11] The segregation of the two phases also limits the contacts between them, creates inhomogeneities in ionic and/or electronic conductivity, which also lead to underutilization of the regions of the electrode having a locally higher impedance. Furthermore, regions with low impedance experience higher current densities, leading to more rapid cell aging.^[12,13] The initial density of the electrode is also critical as well as the pressure applied during cycling.^[14,15] Previous works also revealed a redox lithium exchange mechanism between silicon and graphite, at their interface or through the electrolyte during the lithiation of the two materials (on charge) or during a period of constant voltage at the end of charge.^[16,17] This exchange of lithium and electrons is intensified, facilitated by a large contact surface, or said differently by numerous contacts, between the two materials.^[18]

[a] Dr. C. Meyssonnier, C. Chalard, Dr. N. Goubard-Bretesché, A. Merabet, Dr. N. Dupré, Prof. B. Lestriez

Nantes Université, CNRS, Institut des Matériaux de Nantes Jean Rouxel, IMN, Nantes F-44000, France

E-mail: bernard.lestriez@cnrs-imn.fr

[b] Dr. C. Meyssonnier, C. Chalard, Dr. C. Paireau

Armor Battery Films, 7 Rue de la Pelissière - 44118 La Chevrière

Supporting information for this article is available on the WWW under <https://doi.org/10.1002/batt.202400119>

Several properties of graphite can influence its interactions with silicon, such as the size and shape of particles, their internal porosity, their specific surface area, or even their hardness.^[11,19,20,21] Du et al., observed for mixtures of graphite and a Si-based alloy (with particle sizes ranging from 0.5 to 8 µm, and an average size of 1 µm), an advantage of SFG6L (platelets of 3 µm in diameter on average) compared to MAG-E (angular particles of 20 µm in diameter) in terms of cycling performance, attributed to a more homogeneous electrode morphology and better interconnectivity of the particles.^[19] Jeschull et al. highlighted the advantage of combining graphites of different particle sizes. Wang et al., studied SiO_x/graphite mixtures.^[20] In the case of angular SiO_x particles with a D50 of 7.7 µm, better performance are obtained with a platelet-like graphite SFG15 (D50 at 9 µm) compared to C59, also platelet-like but larger (D50 at 15 µm). In the SiO_x/C59 mixture, the SiO_x particles agglomerate between the large graphite sheets. This conductive network is more easily damaged due to the expansion of SiO_x particles with local agglomeration, while the small size SFG15 graphite with lower anisotropy helps to build a composite electrode with more random and uniform particle distribution, which facilitates the construction of the stable conductive network. Additionally, the expansion of electrodes designed with SFG15 is minimized.^[21] The quality of the electrode formulation, with the choice of the conductive additive, the binder(s), and their quantities, plays also a crucial role in the homogeneity of the operation of the electrodes.^[22,23] Numerous works relate to the selection of the binder and point towards the choice of polyacrylic acid (PAA) and its derivatives.^[24,25] and ref therein

Optimizing the electrodes based on a silicon/graphite mixture is therefore critical, but it is made difficult and complex due to the multiplicity of parameters that come into play. Studies based on numerical simulations are in this sense powerful and very useful,^[26] but their relevance requires to be nourished by exhaustive experimental studies to make the models more reliable. In order to guide all this work relating to the formulation of electrodes, it is necessary to rely on criteria allowing these formulations to be compared rationally.

The importance of contacts between the two phases, silicon and graphite, on the electrochemical behaviour of their electrode is well established by the literature cited above. In practice these contacts can be quantified by their number or their density per unit area for example, as well as by their dimensions in terms of quantity of interface. This quantification of the morphology of an electrode can be determined using tomography characterizations,^[6,27,28] or predicted by numerical simulation.^[26] As mentioned above, in order to optimize *a priori* and therefore more quickly the formulation of the electrodes, it would be useful to know the target to be achieved so that the quantity of contacts between the two phases ensures the best possible electrochemical functioning of the electrode. To this end, we sought to rationalize this key factor by introducing a new parameter for electrode formulation: the contact ratio between the graphitic carbons and silicon phases, which is the ratio between the quantity of surface area developed by the silicon phase, and that by all the graphitic carbons, including

the conductive additive. This contact ratio Ω is calculated according to equation 1

$$\Omega = \frac{\text{powder surface area of graphite \& conductive carbon (m}^2\text{)}}{\text{powder surface area of silicon (m}^2\text{)}} \quad (1)$$

The surface area quantity of each phase is arbitrarily calculated from the specific surface area of each material and its quantity (mass fraction) in the electrode. However, this is only an estimate. The BET surface area likely does not truly reflect the area available for contact between silicon and graphite and carbon particles. The BET surface area also does not reflect the actual area available on the Si powder for binder absorption. Especially the BET surface area of carbon black would be much greater than the actual carbon black area that is accessible to the binder. The assumption made here is that at least the BET surface area should follow the same general trend as both these properties.

The influence and interest of this parameter is studied here on SiO_x/graphite electrodes, containing a mixture of two graphites different in the size and shape of their particles, and containing different quantities and type of carbon additive (spheres vs. carbon nanotubes). In addition, the quantity of polymer binder in these electrodes was adjusted so as to keep another electrode formulation parameter constant: the binder-to-powders coverage ratio, Γ .

$$\Gamma = \frac{\text{binder mass (g)}}{\text{powder surface area (m}^2\text{)}} \quad (2)$$

Indeed, it is known that the mechanical properties of the electrodes depend on the presence of the polymer binder distributed on the surface of the particles and forming bridges between them.^[25] Comparing electrodes containing different mixtures of powders with variable particle sizes while keeping the quantity of binder constant would introduce a bias in the assessment of their performance, because the increase in the total surface area developed by these powders would weaken their mechanical properties. On the contrary, keeping the coverage ratio constant makes it possible to level out the influence of the binder in order to better highlight and rationalize the influence of the contact ratio on the electrodes properties and performance.

Experimental

Materials

All electrode components are industrial grades. The silicon-based material is a silicon oxide covered by graphene sheets (SiO_x) from a graphene supplier (D50≈10 µm, specific surface area ≈1.4 m²g⁻¹, specific capacity ≈1400 mA h g⁻¹). Graphite active materials used are GHDR 15-4 (D90=23 µm, specific surface area ≈4 m²g⁻¹ – Imerys) and SFG6L (D90=5.3–7.3 µm, specific surface area ≈17 m²g⁻¹ – Imerys) with a theoretical capacity of 372 mA h g⁻¹. C-NERGY™ SUPER C45 was used as conductive carbon additive (grit

20 μm =12 ppm, specific surface area $\approx 45 \text{ m}^2 \text{ g}^{-1}$ – Imerys). A commercial solution containing carbon nanotubes (CNT) dispersed in water with carboxymethylcellulose (CMC) was also used as conductive carbon additive. CNT are Graphistrength® C W2-L C from Arkema (specific surface area $^{\text{BET}} \approx 220 \text{ m}^2 \text{ g}^{-1}$). Polyacrylic acid (PAA, Mw=450 000 g mol $^{-1}$ – Sigma-Aldrich) neutralized with a LiOH.H₂O salt (Sigma-Aldrich, white crystal) was used as binder. In addition, the styrene-butadiene rubber (SBR – BM-451B) from Zeon Corporation was used to complete PAA.

Electrode Preparation

Details of anodes composition are gathered in Table 1. Binder solutions for SiO_x/Graphite anode were prepared by mixing PAA and water with a magnetic stirrer. As shown in Table 1, the binder amount has been varied from a slurry to another. However, the higher the binder amount, the more viscous the slurry is. Therefore, in order to prepare slurries with similar viscosity, the binder concentration was adapted, varying between 5.4 and 6.6 wt%. Finally, the pH of PAA solutions was adjusted at 4.0±0.1 with the LiOH.H₂O salt, estimated at ≈ 0.1 wt% of the binder solution and of the final electrodes. CNT solution was added to the binder solution if appropriate.

SiO_x/Graphite electrode slurries were prepared by mixing the binder solution with other electrode components thanks to a planetary

blender (Thinky mixer ARE 250). SiO_x/Graphite balance is kept to 23:77 for all studied compositions. The powder of each electrode component was incorporated successively, and binder solution was then progressively added to form the electrode slurry (mixing steps in Table S1). The slurry was coated onto an 8 μm copper foil and dried according to the following process: 10 min. at 30 °C, a subsequent temperature ramp to reach 110 °C in ≈ 35 min. and finally 30 min. at 110 °C. The wet thickness was adapted for each slurry to obtain a theoretical areal capacity of 5.1±0.2 mA h cm $^{-2}$. After the drying step, electrodes were then calendered at 1.5 tcm $^{-2}$ with a rolling press (Medlab P – Ingecal) at 50 °C to reach a porosity between 35±5%. Porosity was calculated from the components mass fractions and densities thanks to three thickness measurements of each electrode by a micrometer (Mitutoyo).

Finally, 15 mm diameter circular electrodes were punched out and dried 3–4 hours at 100 °C under vacuum in a Büchi before entering the glove box and coin cell assembling.

Electrochemical Measurements

SiO_x/Graphite electrodes were tested in coin cells (dried 8 h at 60 °C) versus metallic lithium. They were assembled in glove box under argon atmosphere. A glass-fibre Whatman GF/D (dried 6 h under vacuum at 250 °C) and a trilayer microporous membrane (PP/PE/PP) Celgard H2010 (dried 2 h under vacuum at 70 °C) were used

Table 1. Weight percentage composition of the electrodes and their contact and coverage ratio.

Name	Ω^{a} [m 2 m $^{-2}$]	Γ^{b} [mg m $^{-2}$]	SiO _x /Gr balance	SFG6 L/GHDR balance	Binder [wt %]			Active material [wt %]			C45 $^{\text{c}}$ [wt %]	CNT [wt %]	
					PAA $^{\text{b}}$	SBR	LiOH	SiO _x	SFG6L	GHDR			
xSFG	0-SFG	16.2	17.7	23:77	0:100	05.9	2.5	<0.0	20.0	00.0	67.5	4.0	N/A
	10-SFG	18.7	17.2		10:90	06.9	2.5	0.1	19.9	06.7	60.4	3.6	
	20-SFG	21.2	16.8		20:80	07.8	2.6	0.1	19.7	13.3	53.2	3.2	
	33-SFG	24.6	16.5		33:67	09.1	2.5	0.1	19.6	22.0	44.1	2.7	
	40-SFG	26.3	16.3		40:60	09.6	2.5	0.1	19.5	26.4	39.5	2.4	
	50-SFG	28.8	16.2		50:50	10.5	2.6	0.1	19.4	32.7	32.7	2.0	
	66-SFG	33.0	16.0		67:33	11.9	2.6	0.1	19.2	43.1	21.6	1.4	
	100-SFG	41.0	15.5		100:0	14.8	2.5	0.2	18.9	63.7	00.0	0.0	
xC45	1-C45	14.4	18.0	23:77	10:90	05.5	2.5	0.1	20.8	07.0	63.1	1.0	N/A
	3.6-C45	Same than 10-SFG				/	/	/	/	/	/	/	
xCNT	0.5-CNT	16.7	18.6	23:77	10:90	6.3 +0.6 ^d	2.5	0.1	20.6	6.9	62.5	N/A	0.5
	1-CNT	20.6	15.3			5.7 +1.2 ^d	2.5	0.1	20.5	6.9	62.2		1.0
	2-CNT	28.9	14.3			6.9 +2.4 ^d	2.5	0.1	19.7	6.8	59.7		2.0

^a Contact ratio, equation (1). Powder surface area were estimated from their BET surface area and their respective mass in the electrode. ^b Coverage ratio, equation (2). The PAA amount was increased to keep the coverage ratio in its optimal range of value.^[25] ^c In order to maintain a reasonable quantity of binder in xSFG series, that of C45 was reduced proportionally to the increase in SFG6L. ^d PAA %wt + CMC %wt. CNT are dispersed in commercial solution containing CMC.

as separators. They were soaked with 200 μL electrolytic solution of 1 M LiPF₆ in ethylene carbonate (EC) and dimethyl carbonate (DMC) 1:1 + 10 wt% fluoroethylene carbonate (FEC). SiO_x/Graphite electrodes were employed as the working electrodes with lithium foil as both counter and reference electrodes. The cycling tests were performed in galvanostatic mode at 23 °C within the potential window of 1–0.01 V versus Li⁺/Li. The theoretical C/D-rate based on the theoretical capacity of 607 mA h g⁻¹ (according to SiO_x/Graphite weight ratio of 23:77) was fixed at C/20 for the first three cycles (full capacity in 20 h). The third cycle was then used to define the experimental capacity of the SiO_x/Graphite electrode in order to apply a real of C/D-rate for next cycles.

A first series of cells was tested to evaluate the cyclability at a rate of C-D/5 for the next 57 cycles after the three cycles of formation. For all cycles, a constant current (CC) followed by a constant voltage (CV) step at the end of the SiO_x/Graphite electrode lithiation are applied. This floating step at 10 mV was maintained until the measured current reached an equivalent of a C/50 value or for a maximum duration of two hours. For the sake of reproducibility, at least two cells were tested for each SiO_x/Graphite electrode formulation, and the results were averaged.

A second series of cells was tested to evaluate C/D-rate effect. The three cycles of formation were applied and then from cycle 4 to 34, we evaluated the effect of the D-rate during delithiation. Lithiation remained at C/5 with a CV period to be limited only by the effect of delithiation. Blocks of five cycles at D/5, D/2, 1D, 2D and 3D were carried out with a final block of three cycles at D/5 with CV. A complete cycle at C-D/5 was carried out between each block to check that the D-rate increase did not degrade the electrode. Finally, the last delithiation at n × D of each block was completed by a delithiation at D/5 in order to apply a treatment on the incremental capacities data (dQ/dV) as explained in the corresponding section. From cycle 35 to 67, we did the same process but on the lithiation (C-rate) with constant D/5 delithiation. In order to properly evaluate the effect of the C-rate in lithiation, the CV step was suppressed at the cut-off potential of 10 mV. An initial block of 3 cycles at C/5 was carried out, followed by blocks of five cycles at C/2, 1C, 2C and 3C, separated by a complete cycle at C-D/5 with CV to check the integrity of the electrode. Finally, six cycles at C/5 were performed at the end. Three without CV period and three with. For clarity purpose, in the following, rates imposed during the delithiation process will be referred to as D-rates and C-rates imposed during the lithiation process will be referred to as C-rates.

Direct Current Internal Resistance (DCIR) measurements were done to get an information about internal resistance of the cell during cycling. For some cycles at C-D/5 rate, a pulse of current was applied during delithiation phase at a potential of 210 mV. Current was increased from D/5 to 1D rate during one second. The internal resistance was deduced from the ratio between the voltage drop (ΔV) and the current one (ΔI).

Electrical Measurements

1.5 diameter electrodes were cropped and calendered with a press to reach different porosities between 10 and 50% per composition. Three measurements of resistivity were done per samples with the electrode resistance measurement system HIOKI – RM2610.

Mechanical Measurements

The Peel Strength Test

The electrode samples were cropped to strips of 15×100 mm. For 180° peeling tests set-up, a double-sided adhesive 3M-468MP tape was stuck on a metal vertical plate where the electrode coating was pasted on. On the other electrode side, current collector was attached to another similar tape. The peeling force was carried out with 180° peeling tests (Zwick Roell Z1010) by pulling that later tape at a speed of 100 mm·min⁻¹ during 80 mm length. We peeled 2 or 3 samples per composition and averaged adhesive force.

The Nanoindentation Test

Nanoindentation tests were performed using a nanoindentation tester (HIT 300, Anton Paar) equipped with a spherical diamond indenter with a curvature radius of 100 μm . The maximum indentation force was adapted for each sample so that the indentation depth was approximately 10% of the thickness.^[29] The measurements were conducted in 'sinus mode' (dynamic mechanical analysis), a frequency of 5 Hz and an amplitude corresponding to 10% of the maximum force was applied during the loading phase, at a constant strain load rate/load of 0.2 s⁻¹. A 120 s creep at maximum force is monitored before unloading. ≈5 indents were measured with a distance of 300 μm (>20×indentation depth) at different locations to exclude influences between the indents.

Scanning Electron Microscopy (SEM) Observations

To observe the morphology of the electrodes before cycling, cuts were made using a cross section polisher (JEOL SM-09010). Then a scanning electron microscope (SEM – JEOL JSM 7600F, Hitachi TM3000) was used to visualize the electrode morphology. Cycled electrodes were previously rinsed by immersion in DMC under argon atmosphere and dried to be then transported in the scanning electron microscope without air exposure. Cuts were made using FIB/SEM ZEISS Cross Beam 550 FIB and images were then acquired.

Analysis of Incremental Capacity Curves

Derivative of the capacity with respect to the voltage data were calculated using the EC-Lab® software (BioLogic). A post-processing of these data was done with a home-made routine written using Python™. The aim of the routine was to treat a significant data quantity to discriminate the capacity contributions of each active material. More details are given in Supporting Information.

Results and Discussion

SEM Characterizations

The electrode morphology of the xSFG series was observed by SEM. SiO_x particles appear in light grey, graphite and carbon black particles in dark grey, and porosity in black for images in backscattered electrons. Figure S1a and b show the surface of the 0 and 100-SFG electrodes, and Figure 1a-d show the cross-sections of the 0-, 10-, 40-, and 100-SFG electrodes, respectively. We can note two differences at electrodes surface. First, although the SiO_x/Graphite balance is the same, the SiO_x is less

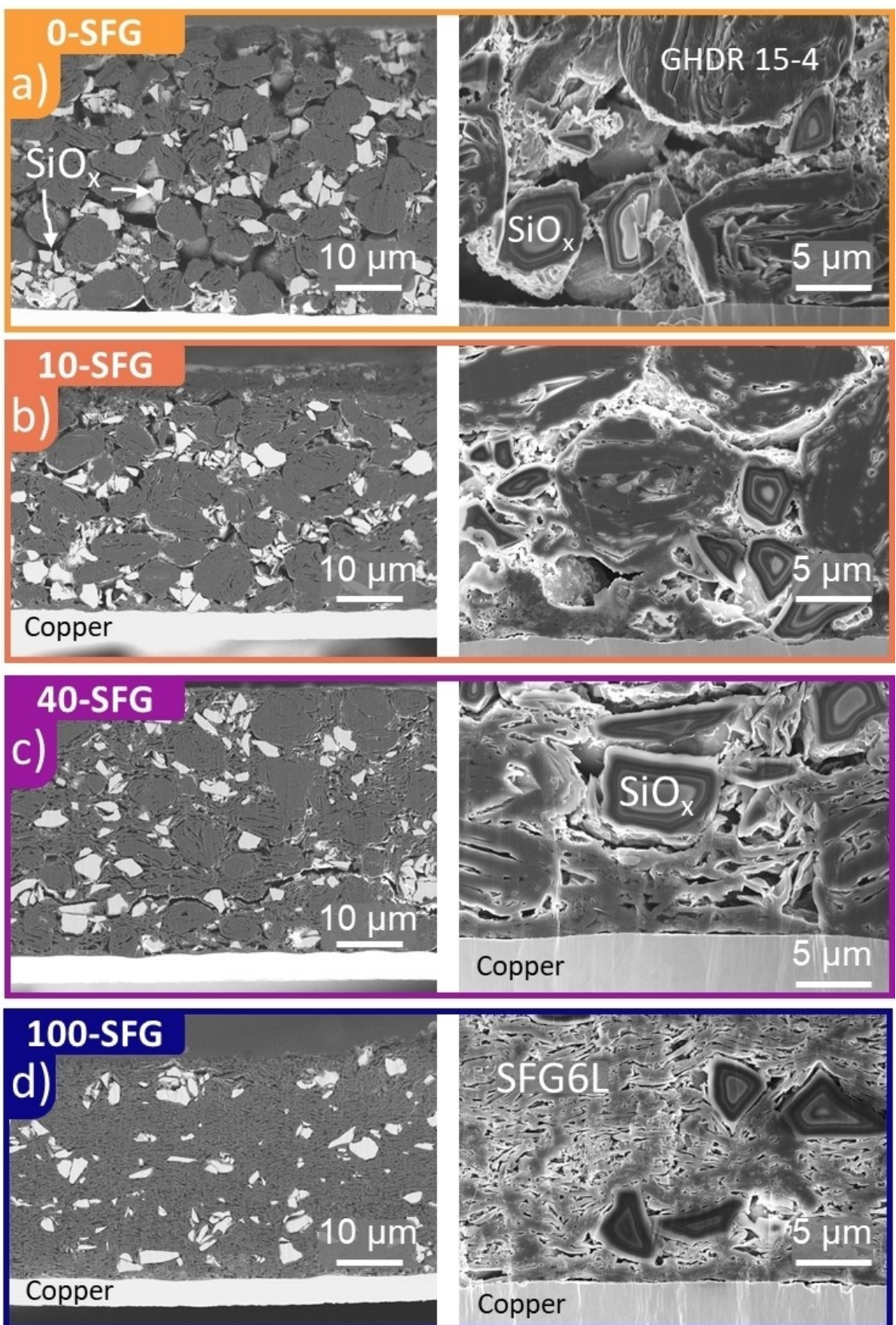


Figure 1. SEM observations of electrode cross section for (a) 0-SFG, (b) 10-SFG, (c) 40-SFG and (d) 100-SFG at $\times 900$ in backscattered (left) electrons and at $\times 4.000$ in secondary electrons (right).

visible in the 100-SFG electrode because it is covered by SFG6L platelet particles. This notion of covering of SiO_x particles by graphite particles is quantified via the contact ratio Ω (Equation 1 and Table 1). Second, although the porosity of these electrodes is quite similar (between 30–40%_{vol}), the pore dimensions are distributed differently. The pores are larger in the 0-SFG electrode. The cross-sections clearly illustrate the differences in shape of GHDR (spherical) and SFG6L (platelet) graphite particles (compare Figure 1a and d). In addition, we find the same morphological differences through the electrodes thickness as at their surface, a greater quantity of contacts, or contact surface area, between the SiO_x and graphite phases with the increase in SFG6L content, as well as a reduction in the average size of the pores. At the highest magnification (x 4000, Figure 1, right column), we can notice some additional details, and in particular distinguish the carbon black C45 phase which appears distributed on the surface of the different types of particles, multiplying the SiO_x /Graphite contacts, or even forming bridges between SiO_x particles, in particular in the 0-SFG electrode. This is why we accounted for carbon black (CB) in the calculation of Ω . Finally, we can note a difference in the quantity of contacts, or contact surface area, between the copper current collector and the electrode films. Compared to the other three, the 0-SFG electrode presents a discontinuity of contacts at this interface, while in the 10-, 40- and 100-SFG electrodes this interface appears continuous due to the presence of a layer of SFG6L which seems to cover the surface of the current collector. The literature shows that all these

morphological differences are likely to affect the cyclability of these electrodes.^[6,30,31,32]

Electrochemical Measurements – Cyclability at D/5-C/5

Figure 2 displays specific capacities versus cycle number for (a) xSFG and (b) xC45/xCNT series. Every electrode composition provides a specific capacity of $775 \pm 12 \text{ mAh g}^{-1}$ for the first lithiation and $619 \pm 5 \text{ mAh g}^{-1}$ during the second one. The latter corresponds to a reversible specific capacity for $\text{SiO}@C \approx 1675 \text{ mAh g}^{-1}$, taking into account the 23:77 $\text{SiO}@C/\text{Gr}$ mass ratio in the composition of the electrode and a specific capacity of 370 mAh g^{-1} for graphite. Figure S2 displays the coulombic efficiency (CE) as a function of the contact ratio for xSFG series. As expected,^[33] the increase in the specific surface area of the GHDR/SFG6L blend leads to a lower initial coulombic efficiency (ICE) from $77.4 \pm 0.3\%$ for 10-SFG to $74.9 \pm 0.2\%$ for 100-SFG. Although all electrodes deliver the same nominal specific capacity at the early stage of cycling, whatever their composition, they then diverge depending on the contact ratio between graphite/carbon black particles and SiO_x ones (Figure 2a–b).

To better assess the effect of this parameter, specific lithiation capacities are plotted Figure 2c as a function of the contact ratio Ω for cycles 2 and 60. This one naturally increases as the SFG6L or C45 or CNT amount increases (Table 1). The retained capacity after 60 cycles strongly increases by $\approx +75 \text{ mAh g}^{-1}$ from 0-SFG to 10-SFG ($\Omega = 16.2$ and $18.7 \text{ m}^2_{\text{Gr+C}} \text{m}^{-2}_{\text{SiO}_x}$ respectively). The capacity gap is

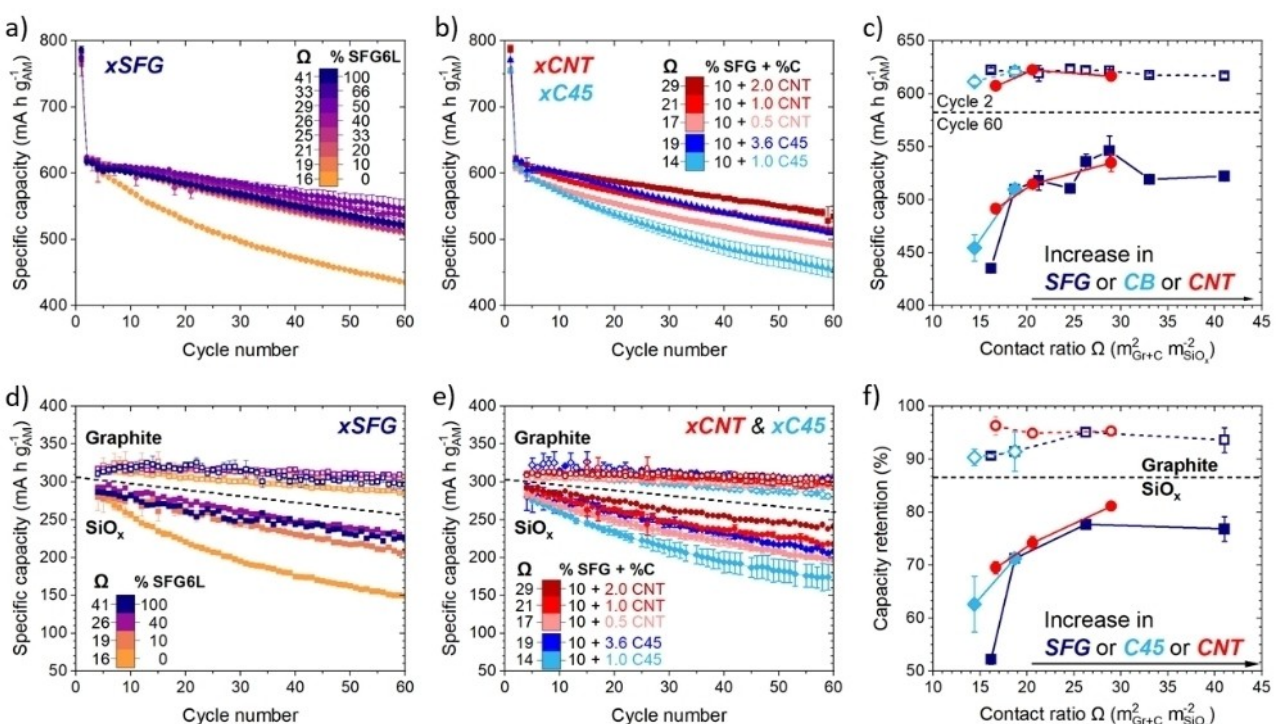


Figure 2. Cyclability at D/5-C/5 of a SiO_x /Graphite electrode for (a) xSFG series, (b) xC45 and xCNT series and (c) Specific capacity vs. Contact ratio for all electrode series at cycle 2 and 60. Specific capacity in the graphite and SiO_x potential windows obtained by incremental capacity analysis for same series (d–e) and (f) their capacity retention vs contact ratio after 60 cycles.

$\approx +55 \text{ mAh g}^{-1}$ between 1-C45 ($14.4 \text{ m}^2_{\text{Gr+C}} \text{m}^{-2}_{\text{SiO}_x}$) and 3.6-C45 (which is also 10-SFG). The capacity gap between 0.5-CNT and 1-CNT electrode (16.7 and $20.6 \text{ m}^2_{\text{Gr+C}} \text{m}^{-2}_{\text{SiO}_x}$) is only $\approx +25 \text{ mAh g}^{-1}$. Further comparing the impact of different carbon species, 0.5-CNT contains only 0.5% _{wt} of CNT but achieves better capacity retention after 60 cycles than 1-C45, containing 1.0% _{wt} of C45, which is also related to a higher contact ratio of the former electrode (16.7 vs. $14.4 \text{ m}^2_{\text{Gr+C}} \text{m}^{-2}_{\text{SiO}_x}$). Overall, the evolution observed for the xSFG, xCB and xCNT series indicates a strong correlation between contact ratio and specific capacity retention, independently of the nature of the carbon. Nevertheless, from 18.7 to $26.3 \text{ m}^2_{\text{Gr+C}} \text{m}^{-2}_{\text{SiO}_x}$, the retained capacity only tends to increase smoothly, culminating after 60 cycles at $546 \pm 14 \text{ mAh g}^{-1}$ at the contact ratio of $28.8 \text{ m}^2_{\text{Gr+C}} \text{m}^{-2}_{\text{SiO}_x}$ for the SFG6L:GHDR balance of 50:50 with 2% _{wt} of C45. With a same contact ratio, the 2-CNT electrode shows a similar capacity, although its composition is very different, with an SFG6L:GHDR balance of 10:90 and 2% _{wt} of CNT. For higher SFG6L:GHDR balance and contact ratio, a slight decrease is observed to $522 \pm 2 \text{ mAh g}^{-1}$ for the electrode 100-SFG only composed with SFG6L as graphite material. These results show a clear improvement in the cyclability of the electrodes with increasing the contact ratio until it reaches an optimal value equal to approximately $26\text{--}29 \text{ m}^2_{\text{Gr+C}} \text{m}^{-2}_{\text{SiO}_x}$. These observations confirm that there are different ways to increase this ratio: graphite type and carbon additive type. Moreover, it highlights the importance of the notion of powder surface area over the raw mass content of graphite/carbon.

As previously underlined, the strategy to work at constant binder-to-powder coverage ratio implies an increase in the amount of PAA to balance the variation in SFG6L:GHDR. However, it is known that such an increase of binder generally increases Si-based electrodes cyclability.^[25] Therefore, the tendency of improved performance with the increase in the contact ratio could be also explained by the increase in the quantity of binder. To rule this hypothesis out, the cyclability of complementary electrodes with constant binder content and variable SFG6L and C45 (and the contact ratio) contents (See Table S2), are presented in Figure S4b–c. The influence of the SFG6L content and contact ratio on the electrochemical performance of these electrodes is unambiguous. There is an improvement of the cyclability with increasing SFG6L content (and therefore contact ratio). But the retained capacities at the 60th cycle are 440 , 480 and 500 mAh g^{-1} for 0-SFG, 10SFG-6PAA and 40SFG-6PAA, respectively (Figure S4c). These performances are clearly poorer than the one shown above for electrodes formulated at the optimized coverage-ratio, which can be linked to their weaker mechanical properties (see below peel test measurements and Figure S4-a).

To shed light on the fading mechanism, we used the incremental capacity curves to separate the capacity obtained from SiO_x and graphite. The methodology for obtaining such values is explained in our previous work and recalled in SI (Figure S3).^[25] Figure 2d shows the delithiation specific capacities in the graphite and SiO_x respective potential windows for 0-, 10-, 40-, 100-SFG and Figure 2e for xC45 and xCNT series. In

all cases, capacity losses are clearly more significant in SiO_x region than in the graphite one, in agreement with previous works.^[21,25] Here again, we distinguish two different behaviours depending on the contact ratio. Above $17 \text{ m}^2_{\text{Gr+C}} \text{m}^{-2}_{\text{SiO}_x}$ electrodes display a capacity retention in graphite region of $93 \pm 2\%$ and $75 \pm 3\%$ in the SiO_x one after 60 cycles. Below this contact ratio, 0-SFG and 1-C45 electrodes display a lower capacity retention of $90 \pm 1\%$ and $57 \pm 7\%$ in the two respective regions (Figure 2f). In addition, the calculation of the graphite capacity using our home-made Python code leads to an over-estimation (See Figure S3 and^[25]). Although the activity potential range of graphite and SiO_x are quite well separated during the oxidation process, there is nevertheless a partial overlap of the two redox phenomena. In fact, $\approx 20\%$ of the SiO_x capacity come from the $10\text{--}260 \text{ mV}_{\text{vs Li+}/\text{Li}}$ at C/20 (Figure S3a) potential range. Therefore, the small loss of capacity in graphite area should be totally or partly due to a loss of SiO_x capacity. It means that the capacity loss of graphite is surely lower than the one measured here and probably non-existent. This result is not consistent with a scenario in which entire parts of the electrode would be disconnected from the electrical network upon cycling. In that case, the graphite contribution would decrease in the same proportion as that of SiO_x , which is not what is observed here. On the contrary, this result clearly indicates that the capacity fading mainly comes from the SiO_x particles electrical disconnection which is congruent with previous works.^[25,34]

It is shown here that the increase of the contact ratio Ω , by increasing the proportion of smaller and flake-shaped graphite or of CB or CNT conductive additives, helps preventing this disconnection. One likely reason is that increasing the numbers of contacts between SiO_x particles and graphite/conductive carbon in the pristine electrode statistically results in reducing the disconnection of SiO_x particles from the rest of the electrode due to their swelling/shrinking during electrochemical cycling. Overall, these results highlight the relevance of the contact ratio as a way to monitor the contact efficiency between SiO_x particles and graphite / conductive carbon.

SEM Post Mortem Characterizations

Post-mortem analyses were made to better understand the capacity fading sources. Note that these observations were however done on electrodes of xSFG series after D- and C-rate study (see section *Rate performance and engineering optimization*). Table 2 gives for these electrodes their initial thicknesses, mass loading, and capacity, as well as their thicknesses after cycling. The swelling (increase in thickness) is highest for 0-SFG ($+29 \mu\text{m}$) and lowest for 10-SFG ($+19 \mu\text{m}$). In order to rationalize this value in relation to the expected expansion with regard to the SiO_x mass loading in these electrodes, this swelling ($\text{in } \mu\text{m}$) is normalized by their initial capacity (in mAh) to give a measurement of their expansion which is expressed in $\mu\text{m mA}^{-1}\text{h}^{-1}$. To interpret this normalization, we assume that the expected expansion is to the first order proportional to the quantity of SiO_x and thus that any difference in expansion

Table 2. Electrodes thicknesses, mass loading and expansion between pristine state and after D/C-rate study (67 cycles) for 0-, 10-, 40-, 100-SFG samples.						
Sample	Contact ratio Ω [m ² m ⁻²]	Thickness [μm]			Mass loading of active materials [mg _{AM} cm ⁻²]	Expansion ^a [μm mA ⁻¹ h ⁻¹]
		Pristine	Aged	Increase		
0-SFG	16.2	79±1	108±1	+29±0	9.3±0.1	2.9±0.0
10-SFG	18.7	70±5	089±4	+19±1	8.3±0.1	2.1±0.1
40-SFG	26.3	75±2	099±6	+22±1	8.6±0.2	2.5±0.3
100-SFG	41.0	73±2	099±2	+26±0	8.2±0.0	2.9±0.0

^a Electrode thickness increase per its initial capacity (Ah). This calculation allows us to eliminate the differences in mass loading between electrodes.

results from an electrode formulation effect. The values are 2.9, 2.1, 2.5, and 2.9 μm mA⁻¹ h⁻¹ for 0-, 10-, 40- and 100-SFG. They show that the introduction of a low content of SFG6L (case of 10-SFG) significantly reduces the expansion, which can be attributed to the lubricating properties of the SFG6L platelets,^[19] also conferring greater plasticity as observed through indentation measurements (see below), promoting the reorganization of the other particles (SiO_x and GHDR) during the expansion and contraction of the electrode under the effect of the compression imposed by the internal pressure of the cell. However, when the SFG6L content is increased beyond 10% in the GHDR/SFG6L mixture, it leads to an increase in expansion.

For further understanding, SEM observations of electrode cross-section of 10- and 100-SFG samples are compared before (Figure 3a–c) and after cycling (Figure 3b–d). In view of the theoretical volume change of +140% for lithiated SiO_x particles, the global structure of the two electrodes appears well preserved after cycling. The swelling mechanism of the electrodes is well discernible for 100-SFG where SFG6L flakes seems more separated from each other after cycling. The swelling of the SFG6L phase is likely a consequence of the volume variations of the SiO_x particles. Although some voids are discernible around the SiO_x particles, which can be evidenced by comparing with the morphology of pristine electrodes (Figure 1d, 3c and 3d) close examination suggests that these SiO_x particles appear to still remain in contact with some SFG6L ones. The swelling mechanism of the 10-SFG electrode is less obvious. Some voids around SiO_x particles are visible in the aged electrode, but some already exist also in the pristine one. However, it can be argued that the swelling of the graphite matrix, which surrounds the SiO_x particles, can be favoured for a high concentration of SFG6L platelets since there are numerous interfaces between them which can be subject to separation (decohesion) under the effect of the swelling of SiO_x particles in their vicinity. Whereas in a matrix rich in GHDR, the interfaces are fewer, and the swelling of the SiO_x particles will not lead to decohesion inside the GHDR particles. The mechanical behaviour during the cycling of these electrodes is certainly complicated to fully understand on the basis of these images and swelling measurements alone, as the morphology of these electrodes is also heterogeneous from the point of view of the nature and size of particles, as well as the distribution of porosities. It is also difficult to discuss these results further because when the coin cells are dismantled,

there is an expansion of the electrodes which are then no longer under pressure.

However, we can conclude that the cyclability of these SiO_x/graphite electrodes is influenced by the density of contacts between these two phases. This is conditioned in the pristine electrode by the contact ratio, and during cycling by the mechanical properties of the matrix which surrounds the SiO_x particles, which depend on the morphology of the graphite particles (platelet vs. sphere and their respective proportions), porosity, and the nature and quantity of binder, as evidenced by peeling and indentation measurements (Figure 4).

Electrical and Mechanical Characterizations

Two different mechanical tests, 180° peel and nanoindentation, were employed to characterize the mechanical properties of the xSFG electrodes series. In the peel test, the stress is mainly tensile, which highlights the adhesive contribution of the polymer at the particle/particle and/or electrode/current collector interfaces. In indentation, it adds to the contribution of the polymer those of the other phases, which can then be highlighted. Remember that our experimental strategy consisted of adjusting the quantity of binder in the formulation of these electrodes so as to keep the coverage ratio as constant as possible (Table 1) in order to level out the contribution of the binder on the mechanical resistance of these electrodes for exacerbate the effect of the characteristics of graphite.

The average peel force, along with the coverage ratio of the xSFG electrodes series, are given in Figure 4a as a function of the contact ratio, Ω . The coverage ratio, Γ , is not exactly constant. It tends to decrease slightly with increasing SFG6L content, varying from 17.7 to 15.5 mg m⁻². Peel strength varies little. Indeed, all values are between 98±16 N m⁻¹ (0-SFG) and 64±5 N m⁻¹ (20-SFG), with a tendency towards a slight decrease with increasing SFG6L content. Visually, the rupture is of adhesive type for the first four electrodes (0- to 40-SFG) and mixed adhesive/cohesive for the last two tested (50- and 100-SFG), Figure S5. These results therefore indicate a slight decrease in mechanical cohesion under tensile stress with the increase in the SFG6L content. However, we can see that the choice of an almost constant coverage ratio made it possible to level the peeling resistance of these electrodes. Indeed, it is generally observed that increasing the binder content in an

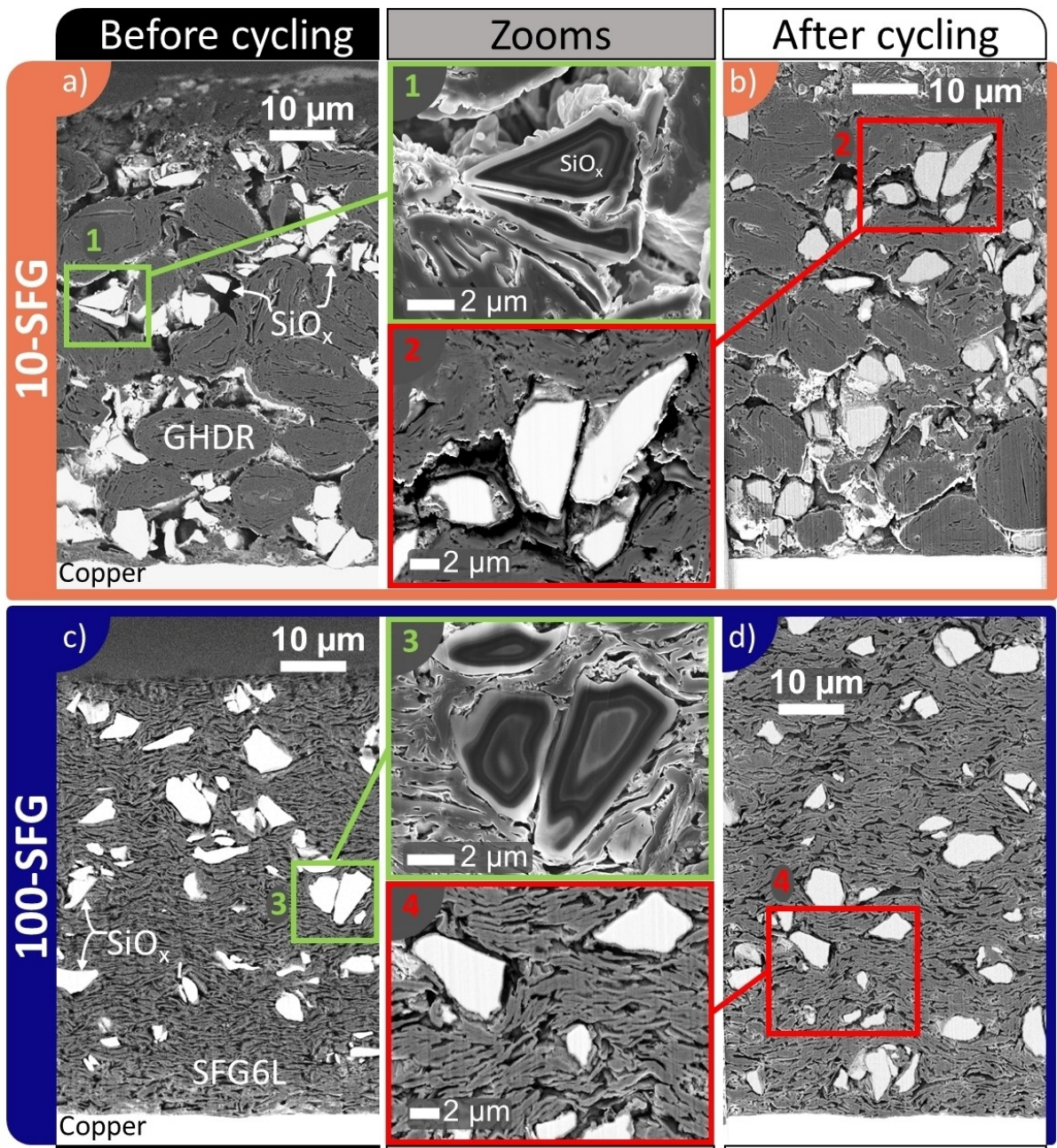


Figure 3. SEM observations of cross section of (a–c) electrodes before cycling and (c–d) electrodes after cycling for 10-SFG and 100-SFG electrodes in backscattered electrons. Some zooms are provided (1–3) in secondary electrons or (2–4) in backscattered electrons.

electrode leads to an increase in its peel strength,^[25] which is not the case here, where the binder content increases from 8.4 to 17.3 wt %. from 0- to 100-SFG. To be convinced of this, the peel resistance of complementary electrodes whose binder content is kept constant while those of SFG6L and C45 vary (see Table S2), are presented in Figure S4a and clearly indicate a decrease of the peel force which validate the approach of working at constant coverage ratio.

Typical indentation curves are presented in Figure S6. Results are presented Figure 4c and d (please note that Figure 4b is discussed later). The dependence of compressive elastic modulus and hardness on porosity is well known and

has been observed for electrodes based on silicon,^[35] LiFePO₄,^[36] and NMC333.^[37] The lower the porosity, the higher the hardness, *H*, and the modulus, *E* are. To facilitate comparison between the different electrode compositions, they were densified at several porosity levels. Figure S7c-d shows the evolution of *H* and *E* of the three electrodes from the *x*SFG series, 0-, 10- and 100-SFG, as a function of the porosity. Both *H* and *E* measure the resistance opposed by the material to its indentation and this by different mechanisms, elastic and plastic. As previously observed, both properties increase with a decrease of the porosity. However, they show no sensible variations with electrode composition. Contrarily, the calcula-

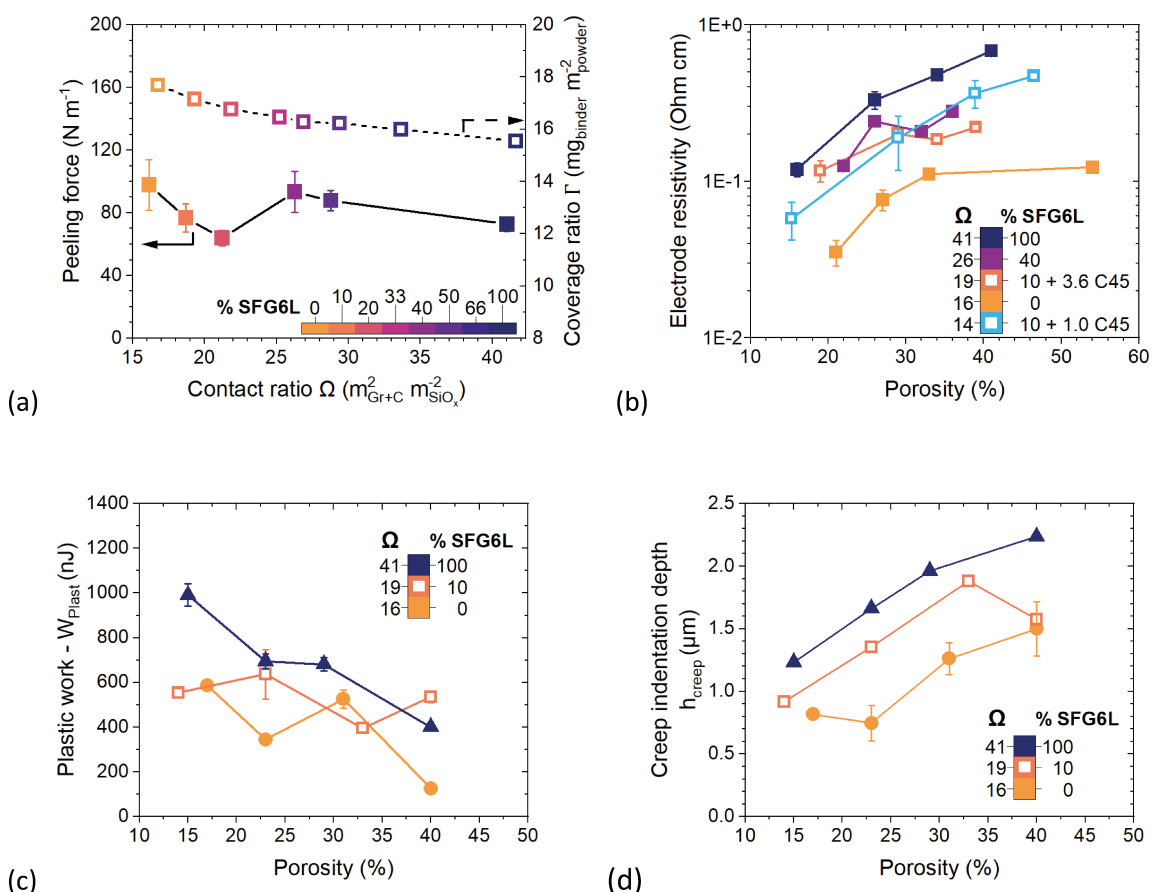


Figure 4. (a) Average peel force (left axis) and binder-to-powders coverage ratio (right axis) vs. contact ratio for the xSFG series. (b) Electrical resistivity vs. electrode porosity for xSFG, xC45 and xCNT series. (c) Plastic part of the mechanical work performed by indentation, and (d) creep indentation depth, as a function of the porosity for 0-, 10- and 100-SFG.

tion of the mechanical work performed by indentation (Figure S8a) shows it is superior for the 100-SFG electrode, because its plastic part, W_{plast} , is higher (Figure 4c), while the elastic parts, W_{elast} , are similar for the three electrodes (Figure S8b). During indentation, the probe compresses the electrode film. The permanent plastic deformation, which remains after unloading, results from irreversible displacements of the particles relative to each other, and possibly from their crushing, simultaneously with the reduction in porosity under the indenter.^[35,38,39] The elastic deformation is that which is recovered during unloading and is related to the elastic compression of the materials under the indenter. In the case of graphite electrodes, the type of graphite is known to affect the behaviour of the electrode film in compression.^[40] The polymer binder also affects these properties (elastic vs. plastic). For example, stiffer binders such as polyacrylic acid and carboxymethyl cellulose increase elasticity compared to more plastic binders such as PVdF.^[41,42] The greater plasticity of the 100-SFG electrodes is attributable to the lubricating properties of the SFG6L platelets^[19] and their greater binder content. It also manifests itself in their greater creeping properties, which occurs under a constant force and thus mainly corresponds to plastic deformation (Figure 4d). The creep indentation depth is defined Figure S6b. It corresponds to an irreversible (plastic) deformation of the electrode. The latter

plot shows that the addition of a small quantity of SFG6L increases a lot the electrode plasticity, when 0- and 10-SFG are compared. This result explains the lower expansion (see Table 2) of the 10-SFG electrode. It indicates that the introduction into the electrode formulation of small graphite particles is favorable to the cyclability of the electrode, on the one hand thanks to a higher initial number of SiO_x/Gr contacts, this statistically allows connectivity between the two phases SiO_x and graphite to be maintained for a greater number of cycles. And on the other hand because a greater number of contacts (which constitute sliding points) increases the plasticity of the electrode subjected to compression imposed by the cell on the electrode. The anisotropy of the SFG6L particles, which favours their sliding, is certainly an advantage relative to the second mechanism.

Figure 4b shows the electrical resistivity of electrodes from xSFG and xC45 series (1- and 3.6-C45) as a function of the porosity. For all compositions, this resistivity decreases with the porosity reduction as expected.^[43] Interestingly the resistivity increases with the increase of the contact ratio and SFG6L content which seems counterintuitive. For example, 0-, 10-, 40- and 100-SFG are respectively $\approx 1.1 \times 10^{-1}$, 1.8×10^{-1} , 2.4×10^{-1} and 4.8×10^{-1} Ohm cm. One might expect that increasing the number of contact points between particles would improve the percolating network and facilitate electron exchange. However,

let us recall that keeping a constant coverage ratio for the xSFG series implies a concomitant increase in binder content when x increases. In this way, the particle/binder/particle interfaces are multiplied throughout the thickness of the electrode. The electrode will therefore be more resistive despite a higher contact ratio, which may explain these resistivity results.

Moreover, the effect of C45 is evaluated with 10% SFG electrodes 1-C45 and 3.6-C45. Resistivity of 3.6-C45 electrode seems less dependent on the porosity (between 1.2 and 2.2×10^{-1} Ohm cm) with low standard deviation. On the opposite, 1-C45 electrodes reach lower resistivity of 0.6×10^{-1} Ohm cm at 15%_{vol} of porosity but a higher one of 4.7×10^{-1} Ohm cm at 47%_{vol} with important standard deviation. At low porosity, contacts between particles are more numerous which minimise the carbon black effect on the percolating network. Then, 1-C45 electrodes are less resistive because of the lower amount of binder compared to the four other electrode formulations (Table 1). On the opposite, at high porosity, poor contacts between particles are less compensated due to the lack of carbon black of 1-C45 electrode compared to 3.6-C45 electrodes. Overall, the resistivity values remain low.

Another reason for these seemingly counterintuitive trends may be an artefact due to the use of the BET surface area to calculate the coverage ratio. The BET surface area of C45 may overestimate the actual surface area accessible to the binder. In comparison, the BET surface area of SFG6L is possibly more representative. This would mean that as SFG6L replaces C45 in the composition of the SFG series electrodes, the actual binder coverage on graphites and SiO_x would increase, leading to an increase in resistivity. However, as the calculated coverage ratio and peel resistance tend to decrease as SFG6L replaces C45 (see Table 1 and Figure 4a), we believe that the most consistent interpretation of the resistivity increase with an increased contact ratio is indeed the increase in the quantity of interfaces which multiply the barriers to overcome to achieve or maintain electronic percolation within the electrodes.

In summary, increasing the proportion of SFG6L in the graphite blend makes it possible to increase the carbons-to-SiO_x contact ratio. The cohesion of the electrodes under tensile (expansion) stress is little affected because the quantity of binder has been adjusted so as to keep the binder-to-powders coverage ratio constant. On the other hand, their plasticity is increased under compressive stress (contraction). Finally, the electrical resistivity increases with the content of SFG6L and C45, and the increase in the contact ratio, which supports the idea that the improvement in cyclability with the increase in the quantity of SFG6L or conductive additive is not attributable to a decrease in the overall electrical resistivity of the electrode, but to the increased durability of connectivity between the two phases due to a greater quantity of SiO_x/Gr contacts, rationalized through the contact ratio.

Rate Performance – Effect of the D- and C-Rate

The study of electrochemical cycling revealed significantly better cyclability for the electrodes of xSFG, xC45 and xCNT

series with a contact ratio higher than $17 \text{ m}^2_{\text{Gr+C}} \text{ m}^{-2}_{\text{SiO}_x}$. Increasing the SFG6L content increases electrode electronic resistivity and leads to smaller pore size and higher tortuosity, which likely increase electrode ionic resistivity, and therefore may have consequences on the electrochemical performance at high rate. To evaluate the influence of this change in the electrode formulation and to identify the best SFG6L:GHDR balance from a broader view than only cyclability, a second series of cells has been tested at different rates. 10-SFG, 40-SFG and 100-SFG compositions were selected as representative of the whole xSFG series. As shown Figure 5a, after the 3 formation cycles at C-D/20, a first part between cycle 4 and 34 is dedicated to the effect of the rate variation during delithiation (D/5, D/2, 1D, 2D and 3D blocks), with the corresponding lithiation rate fixed at C/5 and ending with constant voltage (CV) step at 10 mV (see experimental section). The second part from cycle 35 to 64 is dedicated to the effect of the rate variation during lithiation (C/5, C/2, 1C, 2C and 3C blocks, all without CV step), with the corresponding delithiation rate fixed at D/5. Some complete cycles at C/5 and D/5 are interleaved between D- and C-rates blocks to assess the electrode integrity (check cycles). The 0-SFG electrode has also been tested but its strong capacity fading does not allow relevant comparison with the other electrodes (Figure S9a). Figure 5a gives an overview of the capacity as a function of the D- or C-rate for the different electrodes, while typical discharge and charge curves are shown in Figure S9b-c.

As generally observed for graphite-based negative electrodes, kinetic limitations caused by the increase in C-rate are more severe during lithiation than during delithiation. Here for example, the specific capacity falls at or below $\approx 400 \text{ mAh g}^{-1}_{\text{AM}}$ at 2D rate, while this limit is directly reached for a C/2 rate. Furthermore, it should be noted that in all cases a full capacity is recovered during the C/5 check cycles (15, 21, 27, 32–34, 43, 49, 45, 61, 65–67) indicating that the capacity loss observed for increasing rate is not due to intrinsic degradation of the electrode but rather to electronic and/or ionic kinetic limitations.

Effect of D-rate during delithiation (Figure 5). The percentage of SFG6L in the electrode composition has clearly an impact on the delithiation capacity when the delithiation rate is increased. The last specific delithiation capacity of each D-rate block are shown in Figure 5b as a function of the D-rate. Interestingly, capacities are similar and barely impacted for slow delithiation rate ($\approx 605 \text{ mAh g}^{-1}_{\text{AM}}$ and $\approx 590 \text{ mAh g}^{-1}_{\text{AM}}$ for D/5 and D/2, respectively). The first notable difference appears at 1D, where capacities are still $\approx 550 \text{ mAh g}^{-1}_{\text{AM}}$ for both 10-SFG and 40-SFG electrode, whereas the behaviour of 100-SFG seems to diverge with a stronger capacity decrease to $\approx 470 \text{ mAh g}^{-1}_{\text{AM}}$ showing that the formulation with the most SFG6L content is the first to encounter kinetic limitations. At 2D, the electrode with the intermediate amount of SFG6L electrode (40-SFG), in turn, undergoes a drastic capacity drop and displays a capacity similar to that of the 100-SFG electrode ($\approx 240 \text{ mAh g}^{-1}_{\text{AM}}$), while the 10-SFG electrode is able to retain a capacity of $\approx 360 \text{ mAh g}^{-1}_{\text{AM}}$. Finally, for faster D-rate (3D) all capacities are similarly low at $\approx 110 \pm 25 \text{ mAh g}^{-1}_{\text{AM}}$.

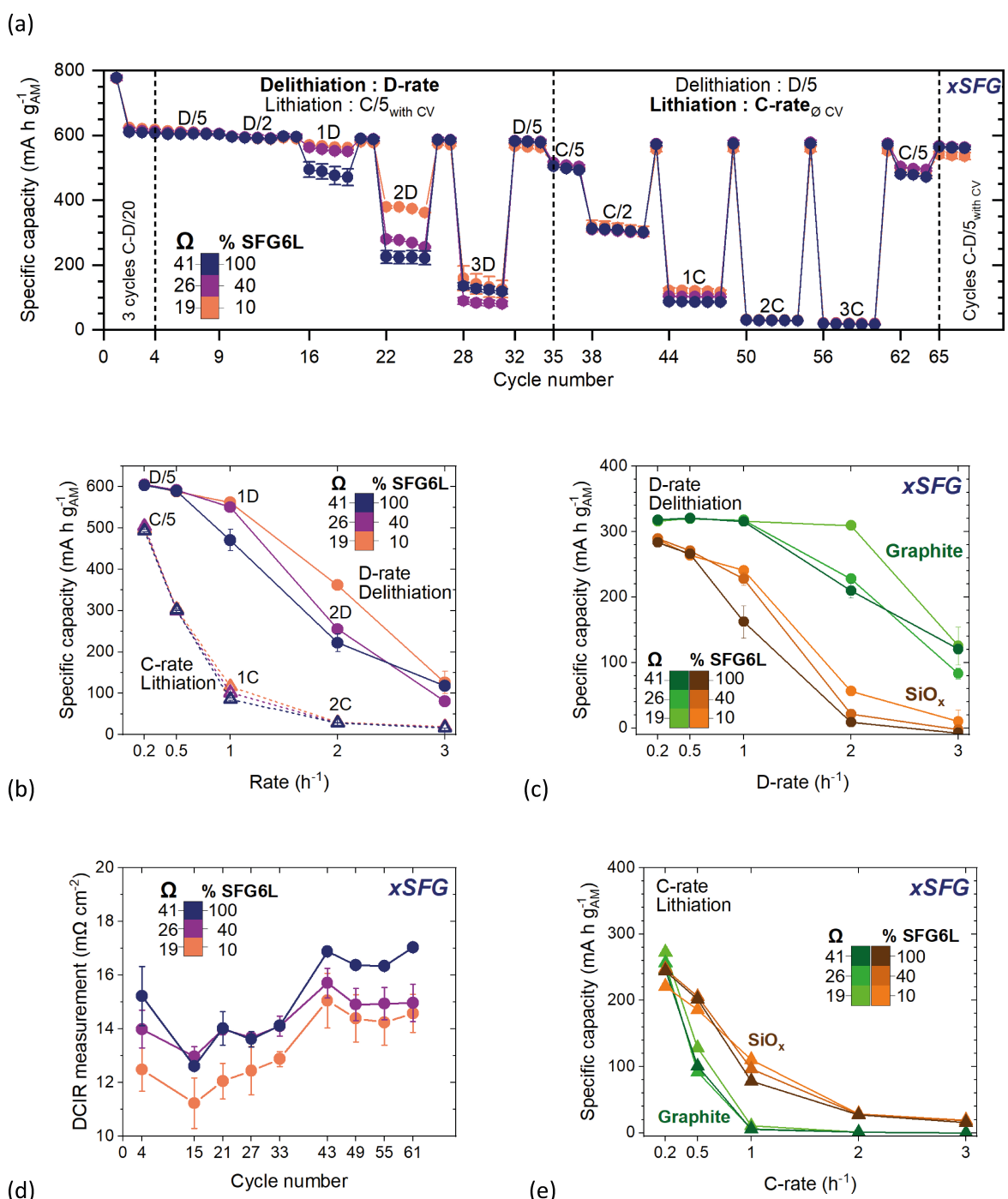


Figure 5. (a) Specific capacity vs cycle number at different D-rates but constant C/5 and then at different C-rates but constant D/5, for 10-, 40- and 100-electrodes from xSFG series; (b) Electrode specific capacity vs cycling rate; (c) Specific capacity in the graphite and SiO_x potential windows vs cycling rate for different D-rates; (d) Internal resistance measured by DCIR measurement vs cycle number; (e) Specific capacity in the graphite and SiO_x potential windows vs Cycling rate different C-rates.

Numerous works have shown that the performance at high rate in delithiation of high capacity graphite electrodes ($> 3 \text{ mAh cm}^{-2}$) depends on the limitations imposed by the architecture of the electrode on the diffusion of the lithium salt in the electrolyte.^[44,45,46,47] In fact, a lithium salt concentration gradient appears and becomes more marked as the current density is higher and the diffusion of salt is restricted. In half-

cell configuration, it has been shown that during delithiation (in oxidation), the salt concentration can increase significantly above its average concentration in the graphite electrode, while in the vicinity of the lithium counter-electrode the salt concentration drops, causing a sudden increase in the cell potential which puts an end to delithiation process. These limitations are aggravated and performance reduced with

increasing thickness and decreasing porosity of the graphite electrode. At equal porosity and thickness, the use of platelet particles increases the tortuosity of the diffusion paths compared to spherical particles and further penalizes performance at high rate. The electronic conductivity of the graphite electrode is generally considered non-limiting, particularly due to the high intrinsic conductivity of graphite. However, in the case of large particles ($>10\text{ }\mu\text{m}$), a previous work shows an improvement in performance at high rate if carbon black is added. The multiplication of the contacts points between the large graphite particles and carbon black reduces the resistance to the charge transfer reaction (insertion/deinsertion of lithium).^[44,48] However, here the rate performance decreases with increasing the contact ratio. Therefore, differences observed between 10-SFG, 40-SFG and 100-SFG compositions can be explained by the higher tortuosity of the electrodes containing a higher concentration of SFG6L.

To further understand these kinetic limitations, we discriminated the capacity drops attributable to graphite and to SiO_x and monitored their evolution when the delithiation current increases. A specific methodology was followed to evaluate D-rate effect (during delithiation) because our post-processing of incremental capacity data is done on delithiation curves. Details are given in the Supporting Information (Figure S9g, Equation S6–S7). Results are shown Figure 5c where graphite and SiO_x capacities are plotted as a function of the D-rate for each composition. Firstly, each composition delivered the same graphite and SiO_x capacities of $317 \pm 1\text{ mAh g}^{-1}\text{ AM}$ and $287 \pm 3\text{ mAh g}^{-1}\text{ AM}$ at D/5, respectively. This result is in agreement with the fact that electrodes are not degraded yet at cycle 8 and because the SiO_x /Graphite balance is similar for all composition (Table 1) and is such that 52% of the total capacity is provided by the graphite phase, and 48% by the SiO_x one at D/5-C/5. Graphite capacity remains high ($\approx 315\text{ mAh g}^{-1}\text{ AM}$) and stable for all electrodes until a 1D rate is reached. This capacity is further retained at 2D for 10-SFG, whereas capacities drop to 228 and $210\text{ mAh g}^{-1}\text{ AM}$ for 40-SFG and 100-SFG, respectively. Then all electrode compositions yield low graphite capacities of $\approx 80\text{--}120\text{ mAh g}^{-1}\text{ AM}$ at a 3D rate. The capacities of SiO_x are more affected by the D-rate during delithiation. The same pattern of capacity drop is found as for the electrode total capacity. A small drop of $\approx 15\text{ mAh g}^{-1}\text{ AM}$ is observed from D/5 to D/2 in all cases. A comparable drop $\approx 15\text{ mAh g}^{-1}\text{ AM}$ is observed from D/2 to 1D for 10-SFG and 40-SFG while the behaviour of the 100-SFG electrode diverges strongly with an increase of the capacity drop $\approx 100\text{ mAh g}^{-1}\text{ AM}$. At 2D the SiO_x capacity decreases dramatically to 56, 21 and $9\text{ mAh g}^{-1}\text{ AM}$ for 10-SFG, 40-SFG and 100-SFG respectively. At this rate, the capacity delivered by SiO_x in the 10-SFG appears however to be still the highest. At 3D, SiO_x capacity reaches almost equally low values for all compositions indicating that no capacity can be recovered from the SiO_x at this rate anymore.

The comparative evolution of the SiO_x and graphite capacity drops induced by increasing the D-rate indicates unambiguously that the former is preferentially affected than the latter, which is due to the higher delithiation potential of SiO_x compared to graphite. Interestingly, the GHDR/SFG6L balance

clearly affects the SiO_x as well as the electrode total capacity drops, again pinpointing the advantage of having less SFG6L in the electrode composition to minimize tortuosity restrictions to lithium salt diffusion.

Effect of C-rate during lithiation. The last specific lithiation capacity of each C-rate block are shown in Figure 5b as a function of the C-rate. The measured capacities are $\approx 500\text{ mAh g}^{-1}\text{ AM}$ at C/5, $\approx 300\text{ mAh g}^{-1}\text{ AM}$ at C/2, $\approx 30\text{ mAh g}^{-1}\text{ AM}$ at 2C and $\approx 20\text{ mAh g}^{-1}\text{ AM}$ at 3C. While the amount of SFG6L in the electrode impacts the delithiation kinetics, the lithiation appears to be less sensible to the rate variation. A small difference between electrode compositions is noticeable only at 1C where capacities are $116 \pm 6\text{ mAh g}^{-1}\text{ AM}$, $101 \pm 1\text{ mAh g}^{-1}\text{ AM}$ and $85 \pm 2\text{ mAh g}^{-1}\text{ AM}$ for 10-SFG, 40-SFG and 100-SFG respectively. During lithiation (reduction) and for graphite electrodes, limitations to diffusion of the lithium salt also occur but they have less influence than the ohmic drop that decreases the cell potential down to its cut-off value at 10 mV. The phenomenon affecting the most this ohmic drop in a half-cell is the one at the lithium electrode, which starts to be significant from current density of $\approx 1\text{ mA cm}^{-2}$ and higher.^[45] In the present study, such current densities are effectively achieved at C/5 to reach $\approx 15\text{ mA cm}^{-2}$ at 3C (Table S3) due to the high areal capacity of $\approx 5\text{ mAh cm}^{-2}$ of the electrodes. However, metallic lithium is the same for all coin cells, meaning that any differences observed between 10-SFG, 40-SFG and 100-SFG electrodes rather come from differences in their composition. For further analysis, internal resistance was estimated by DCIR measurements (in delithiation). Results are shown in Figure 5d. The internal resistance globally decreases between cycle 4 and cycle 15 for all compositions and then increases upon cycling until cycle 61. Cycle 4 is the first cycle at C-D/5 after the three activation cycles at C-D/20. An adaption (formation) of the electrode is therefore observed during activation which is materialized by this internal resistance decrease. The increase in internal resistance with cycling is significant of the mechanical degradation of the electrodes and of the SEI growth. The increase of the internal resistance when going from 10-SFG, to 40-SFG, and then to 100-SFG is in line with several observations: (i) the increase of the electrical resistivity (Figure 4b) and (ii) the larger expansion (Table 2).

Again, we discriminated the capacity drops attributable to graphite and to SiO_x upon integration of incremental capacity curves (methodology in the Supporting Information, Figure S3). Results are shown Figure 5e where graphite and SiO_x capacities are plotted as a function of the C-rate for each composition. Firstly, it can be observed that each composition did not deliver the same graphite and SiO_x capacities at C/5 contrarily to the delithiation study (see Figure 5c). The SiO_x contribution to the capacity of the 10-SFG electrode is lower of $\approx 23\text{ mAh g}^{-1}\text{ AM}$ compared to the two others, which is due to its poorer cyclability as previously observed (Figure 2a–c). The graphite capacities are lower than measured in delithiation at D/5, which is due to the CV step removal (See explanation in Supporting information Figure S10). This drop of capacity caused by the CV step removal comes from the graphite and is linked to the internal resistance increase caused by SFG6L. Secondly, it can

be observed that the capacity drop is more severe for graphite than for SiO_x with the C-rate increase (Figure 5e), which is due to the lower lithiation potential of graphite compared to SiO_x . Graphite capacities are $\approx 100 \text{ mAh g}^{-1}$ at C/2, then reach 7–3 mAh g^{-1} at 1C and become close to zero at 2C and 3C. On the contrary, capacity drop of SiO_x is smoother than graphite with capacities of $\approx 200 \text{ mAh g}^{-1}$ at C/2, $\approx 100 \text{ mAh g}^{-1}$ at 1C, $\approx 25 \text{ mAh g}^{-1}$ at 2C and $\approx 15 \text{ mAh g}^{-1}$ at 3C respectively. Interestingly, SiO_x appears as the only active “species” contributing to the capacity of the composite SiO_x/Gr anode for cycling rate faster than 1C. In addition, the influence of SFG6L amount is noticeable on SiO_x capacity, in particular at 1C, as shown by the shape of capacity drop curve as a function of the C-rate. The lower internal resistance observed for lower SFG6L content (Figure 5d) supports the smoother capacity drop for the 10-SFG electrode. Thus, the determination of graphite and SiO_x capacities allows monitoring the effect of the SFG6L:GHDR balance according to the C-rate effect whereas electrodes capacities were identified as similar. To fully evaluate $\text{SiO}_x/\text{graphite}$ anode formulation effect at high C-rates, full-cell configuration tests would be necessary, but they involve other issues such as pre-lithiation or the consumption of the limited reservoir of Li ions in the continuous creation of solid electrolyte interphase (SEI) and are out of the scope of the present study.

Engineering Optimization

The best specific capacity retention (in mAh per gram of active material) of these $\text{SiO}_x/\text{graphite}$ electrodes is obtained once their two formulation parameters, namely the binder-to-powder coverage ratio (Γ) and the graphite-to- SiO_x surface contact ratio (Ω), are adjusted to their critical values, about $18 \text{ mg}_{\text{PAA+SBR}} \text{ m}^2_{\text{Gr+C+SiO}_x}$ and $26\text{--}29 \text{ m}^2_{\text{Gr+C}} \text{ m}^{-2}_{\text{SiO}_x}$, respectively. From an applied point of view, more critical than the specific capacity are the gravimetric and volumetric capacities. For example, since the binder is an inactive constituent, it is however important to verify that an increase in its content in the xSFG series formulation does not improve the cyclability of

the electrode at the expense of the gravimetric capacity. This is explored and confirmed in Figure 6a in which the gravimetric capacity (taking into account half of the current collector mass) is given after 60 cycles. After 60 cycles, the best performance is achieved above 10% of SFG6L ($\Omega = 18.7 \text{ m}^2_{\text{Gr+C}} \text{ m}^{-2}_{\text{SiO}_x}$) in the GHDR/SFG6 blend and culminate for 40–50% (26.3–28.8 $\text{m}^2_{\text{Gr+C}} \text{ m}^{-2}_{\text{SiO}_x}$). (Figure 6a). Further, it is possible to calculate the volumetric capacities of these electrodes, which is done by considering their thicknesses in their pristine and aged states (as given in Table 2). Figure 6b shows the corresponding volumetric capacities. For the pristine state, the reversible capacity at the 2nd cycle and the pristine electrode thickness are considered, while for the aged state, they are the reversible capacity at the 60th cycles and the aged electrode thickness. Here, the best performance is obtained for 10 and 40% (26.3–28.8 $\text{m}^2_{\text{Gr+C}} \text{ m}^{-2}_{\text{SiO}_x}$) of SG6L. The further decrease of the volumetric capacities along the increase in amount of SFG6L (40-SFG and 100-SFG) most probably stems from the increase in inactive materials in the electrode to keep constant coverage ratio and larger dilation. Finally, we saw that the use of SFG6L in the electrode above 10% introduces some limitations for use at higher C/D-rates. Therefore, an optimal composition to reach at the same time high gravimetric and volumetric capacities, good cyclability and rate performance is around 20% SFG6 L, corresponding to a contact ratio of $21 \text{ m}^2_{\text{Gr+C}} \text{ m}^{-2}_{\text{SiO}_x}$ and a coverage ratio of $17 \text{ mg}_{\text{PAA+SBR}} \text{ m}^2_{\text{Gr+CB+SiO}_x}$.

Conclusions

In a $\text{SiO}_x/\text{graphite}$ electrode, variations in volume of the SiO_x lead during cycling to its progressive electrical disconnection and a loss of capacity. In order to counteract this phenomenon, it is possible to play on the nature of the graphite (SFG6L platelets vs. spherical GHDR) and the conductive additives (C45 carbon black vs. CNT), as well as on their respective proportions. To rationalize and facilitate the optimization of electrode formulations, we have introduced the contact ratio between the silicon and graphitic carbons phases.

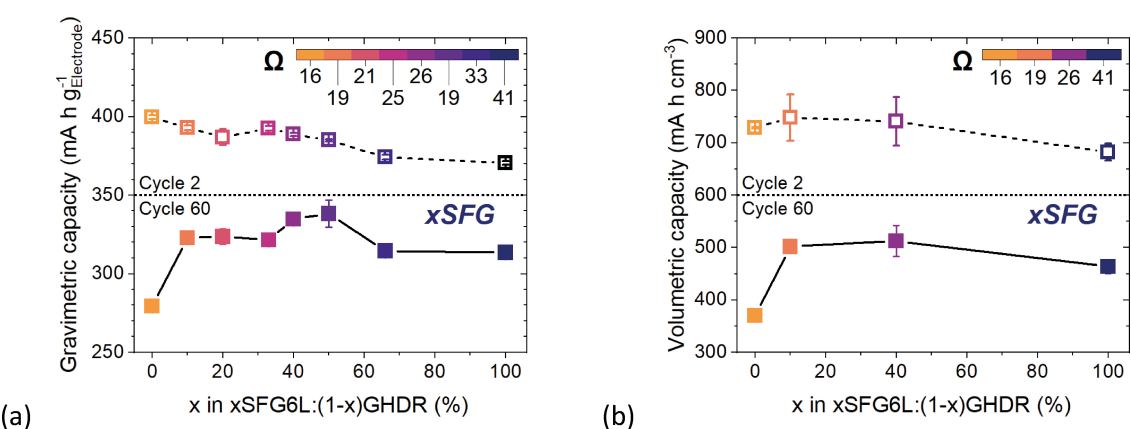


Figure 6. (a) Gravimetric capacity (in mAh per g of electrode) and (b) volumetric capacity (in mAh per cm^3 of electrode) as a function of the SFG6L/GHDR balance. Half of the copper current collector is included in gravimetric capacity but is not considered for volumetric one.

We have shown that its increase, via increasing the proportion of SFG6L or that of C45, or even the substitution of C45 by CNTs, makes it possible to significantly minimize the capacity loss in cycling of the electrodes at the critical value of $17 \text{ m}^2_{\text{Gr+C}} \text{m}^{-2}_{\text{SiO}_x}$. The improvement in cyclability is attributable to the increase in the quantity of $\text{SiO}_x/\text{carbon}/\text{graphite}$ contacts and the increase in the mechanical plasticity of the electrodes under compressive stress. Increasing the contact ratio to $30 \text{ m}^2_{\text{Gr+C}} \text{m}^{-2}_{\text{SiO}_x}$ makes it possible to further increase the cyclability of the electrodes, without this being detrimental in terms of gravimetric and volumetric capacity. But this is at the expense of their rate performance, probably due to the increase in the tortuosity of the porosity with the increase in the SFG6L platelets content, which penalizes the diffusion of the electrolyte salt, and due to the increase in electrode resistance with increasing number of interfaces. Looking at all the performance indicators, it appears that the value of $20 \text{ m}^2_{\text{Gr+C}} \text{m}^{-2}_{\text{SiO}_x}$ is optimal for the contact ratio.

This appears to be an essential and practical parameter in the formulation of electrodes to facilitate their optimization. Indeed, an optimal contact ratio estimated from preliminary work can then be used to design a priori the formulation of an electrode based on a new type of silicon material. This approach should therefore facilitate the comparison of different grades (for example different particle sizes) of a given silicon material, or the optimization of the content of conductive additives.

Equation 1 estimate the contact ratio with the BET surface area of the materials. However, the actual area of contacts in an electrode would be greatly affected by the electrode porosity. This is because as the porosity is decreased, a lower amount of the surface area of the powders would be exposed to porosity. Therefore, the amount of actual contact area between powders will increase as porosity is decreased. Along this line of thinking, it would be interesting to include in a later study the effect of calendering (i.e. increasing total particle-particle contact) on cycling performance. This increase in contact area would be offset by reduced electrolyte penetration into the electrode. Moreover, FEC effectiveness may change depending on the surface area of the powders exposed to the electrolyte. Therefore, there should be some porosity that results in a maximum cycling performance.

Acknowledgements

M. Deleplanque and C. Busson are warmly thanked for fruitful discussions.

Conflict of Interests

The authors declare no conflict of interest.

Data Availability Statement

The data that support the findings of this study are available from the corresponding author upon reasonable request.

- [1] M. Armand, P. Axmann, D. Bresser, M. Copley, K. Edström, C. Ekberg, D. Guyomard, B. Lestriez, P. Novák, M. Petranikova, W. Porcher, S. Trabesinger, M. Wohlfahrt-Mehrens, H. Zhang, *J. Power Sources* **2020**, 479, 228708.
- [2] M. N. Obrovac, V. L. Chevrier, *Chem. Rev.* **2014**, 114, 11444.
- [3] X. Zhu, B. Liu, J. Shao, Q. Zhang, Y. Wan, C. Zhong, J. Lu, *Adv. Funct. Mater.* **2023**, 33, 2213363.
- [4] M. Wetjen, D. Pritzl, R. Jung, S. Solchenbach, R. Ghadimi, H. A. Gasteiger, *J. Electrochem. Soc.* **2017**, 164, A2840.
- [5] M. Wetjen, S. Solchenbach, D. Pritzl, J. Hou, V. Tileli, H. A. Gasteiger, *J. Electrochem. Soc.* **2018**, 165, A1503.
- [6] V. Vanpeene, J. Villanova, A. King, B. Lestriez, E. Maire, L. Roué, *Adv. Energy Mater.* **2019**, 9, 1803947.
- [7] S. Müller, M. Lippuner, M. Verezhak, V. De Andrade, F. De Carlo, V. Wood, *Adv. Energy Mater.* **2020**, 10, 1904119.
- [8] C. Kang, Y. W. Cho, *J. Power Sources* **2021**, 485, 229311.
- [9] V. Vanpeene, P. Soucy, J. Xiong, N. Dupré, B. Lestriez, L. Roué, *J. Power Sources* **2021**, 498, 229904.
- [10] E. Moyassari, L. Streck, N. Paul, M. Trunk, R. Neagu, C.-C. Chang, S.-C. Hou, B. Märkisch, R. Gilles, A. Jossen, *J. Electrochem. Soc.* **2021**, 168, 020519.
- [11] S. Chae, S. Choi, N. Kim, J. Sung, J. Cho, *Angew. Chem. Int. Ed.* **2020**, 59, 110.
- [12] R. E. Ruther, K. A. Hays, S. J. An, J. Li, D. L. Wood, J. Nanda, *ACS Appl. Mater. Interfaces* **2018**, 10, 18641.
- [13] C. L. Berhaut, M. Mirolo, D. Z. Dominguez, I. Martens, S. Pouget, N. Herlin-Boime, M. Chandesris, S. Tardif, J. Drnec, S. Lyonnard, *Adv. Energy Mater.* **2023**, 13, 2301874.
- [14] V. Müller, R.-G. Scurtu, K. Richter, T. Waldmann, M. Memm, M. A. Danzer, M. Wohlfahrt-Mehrens, *J. Electrochem. Soc.* **2019**, 166, A3796.
- [15] I. Profatilova, E. De Vito, S. Genies, C. Vincens, E. Gutel, O. Fanget, A. Martin, M. Chandesris, M. Tulodziecki, W. Porcher, *ACS Appl. Energ. Mater.* **2020**, 3, 11873.
- [16] J. Moon, H. C. Lee, H. Jung, S. Wakita, S. Cho, J. Yoon, J. Lee, A. Ueda, B. Choi, S. Lee, K. Ito, Y. Kubo, A. C. Lim, J. G. Seo, J. Yoo, S. Lee, Y. Ham, W. Baek, Y.-G. Ryu, I. T. Han, *Nat. Commun.* **2021**, 12, 2714.
- [17] Y. Zhang, W. Wang, Y. Zhao, X. Zhang, H. Guo, H. Gao, D. Xu, Y. Zhao, G. Li, J. Liang, S. Xin, Y. Guo, *Adv. Funct. Mater.* **2024**, 34, 2310309.
- [18] J. Y. Kim, S. Jung, S. H. Kang, J. Park, M. J. Lee, D. Jin, D. O. Shin, Y. Lee, Y. M. Lee, *Adv. Energy Mater.* **2022**, 12, 2103108.
- [19] Z. Du, R. A. Dunlap, M. N. Obrovac, *J. Electrochem. Soc.* **2014**, 161, A1698.
- [20] F. Jeschull, Y. Surace, S. Zürcher, G. Lari, M. E. Spahr, P. Novák, S. Trabesinger, *J. Electrochem. Soc.* **2020**, 167, 100535.
- [21] C. Wang, T. Ma, X. Liu, Z. Liu, Z. Chang, J. Pang, *Batteries* **2023**, 9, 78.
- [22] B. L. Armstrong, K. A. Hays, R. E. Ruther, W. B. Hawley, A. Rogers, I. Greeley, K. A. Cavallaro, G. M. Veith, *J. Power Sources* **2022**, 517, 230671.
- [23] M. Wetjen, M. Trunk, L. Werner, R. Gernhäuser, B. Märkisch, Z. Révay, R. Gilles, H. A. Gasteiger, *J. Electrochem. Soc.* **2018**, 165, A2340.
- [24] J. Xiong, N. Dupré, D. Mazouzi, D. Guyomard, L. Roué, B. Lestriez, *ACS Appl. Mater. Interfaces* **2021**, 13, 28304.
- [25] C. Meyssonnier, A. Merabet, N. Dupré, C. Paireau, B. Lestriez, *Small Methods* **2023**, 2301370.
- [26] D. Zapata Dominguez, B. Mondal, M. Gaberscek, M. Morcrette, A. A. Franco, *J. Power Sources* **2023**, 580, 233367.
- [27] C. R. Hernandez, A. Etiemble, T. Douillard, D. Mazouzi, Z. Karkar, E. Maire, D. Guyomard, B. Lestriez, L. Roué, *Adv. Energy Mater.* **2018**, 8, 1701787.
- [28] F. Cadiou, T. Douillard, N. Besnard, B. Lestriez, E. Maire, *J. Electrochem. Soc.* **2020**, 167, 100521.
- [29] M. Conte, A. Tournier-Fillon, E. Frank, *n.d.*
- [30] Z. Zheng, Z. Liu, P. Wang, Y. Li, *J. Energy Storage* **2021**, 43, 103190.
- [31] C. Busson, M.-A. Blin, P. Guichard, P. Soudan, O. Crosnier, D. Guyomard, B. Lestriez, *J. Power Sources* **2018**, 406, 7.
- [32] Z. Guo, L. Zhou, H. Yao, *Mater. Des.* **2019**, 177, 107851.
- [33] P. Novák, F. Joho, M. Lanz, B. Rykart, J.-C. Panitz, D. Alliata, R. Kötz, O. Haas, *J. Power Sources* **2001**, 97–98, 39.
- [34] I. Choi, M. J. Lee, S. M. Oh, J. J. Kim, *Electrochim. Acta* **2012**, 85, 369.
- [35] Y. Wang, Q. Zhang, D. Li, J. Hu, J. Xu, D. Dang, X. Xiao, Y. Cheng, *Adv. Energy Mater.* **2018**, 8, 1702578.

- [36] T. Sedlatschek, M. Krämer, J. S. K.-L. Gibson, S. Korte-Kerzel, A. Bezold, C. Broeckmann, *J. Power Sources* **2022**, *539*, 231565.
- [37] E. N. Primo, M. Chouchane, M. Touzin, P. Vazquez, A. A. Franco, *J. Power Sources* **2021**, *488*, 229361.
- [38] R. Li, W. Li, A. Singh, D. Ren, Z. Hou, M. Ouyang, *Energy Storage Mater.* **2022**, *52*, 395.
- [39] J. Zhu, W. Li, T. Wierzbicki, Y. Xia, J. Harding, *Int. J. Plast.* **2019**, *121*, 293.
- [40] C.-W. Wang, Y.-B. Yi, A. M. Sastry, J. Shim, K. A. Striebel, *J. Electrochem. Soc.* **2004**, *151*, A1489.
- [41] Y.-S. Park, E.-S. Oh, S.-M. Lee, *J. Power Sources* **2014**, *248*, 1191.
- [42] E. M. C. Jones, Ö. Ö. Çapraz, S. R. White, N. R. Sottos, *J. Electrochem. Soc.* **2016**, *163*, A1965.
- [43] K. A. Striebel, A. Sierra, J. Shim, C.-W. Wang, A. M. Sastry, *J. Power Sources* **2004**, *134*, 241.
- [44] H. Buqa, D. Goers, M. Holzapfel, M. E. Spahr, P. Novák, *J. Electrochem. Soc.* **2005**, *152*, A474.
- [45] S. Malifarge, B. Delobel, C. Delacourt, *J. Electrochem. Soc.* **2018**, *165*, A1275.
- [46] K.-H. Chen, M. J. Namkoong, V. Goel, C. Yang, S. Kazemiabnavi, S. M. Mortuza, E. Kazyak, J. Mazumder, K. Thornton, J. Sakamoto, N. P. Dasgupta, *J. Power Sources* **2020**, *471*, 228475.
- [47] M. Parmananda, C. Norris, S. A. Roberts, P. P. Mukherjee, *ACS Appl. Mater. Interfaces* **2022**, *14*, 18335.
- [48] J. Hu, S. Zhong, T. Yan, *J. Power Sources* **2021**, *508*, 230342.

Manuscript received: February 24, 2024

Revised manuscript received: April 12, 2024

Accepted manuscript online: April 15, 2024

Version of record online: May 8, 2024